RSC Advances

PAPER

View Article Online
View Journal | View Issue

Cite this: *RSC Adv.*, 2023, **13**, 26918

Defect- and oxygen-rich nanocarbon derived from solution plasma for bifunctional catalytic activity of oxygen reduction and evolution reactions†

Hye-min Kim,[a] Byung-chul Cha[b] and Dae-wook Kim *[b]

Received 31st July 2023
Accepted 4th September 2023

DOI: 10.1039/d3ra05164a

rsc.li/rsc-advances

The oxygen reduction reaction (ORR) and oxygen evolution reaction (OER) are key for renewable energy systems, including metal–air batteries, fuel cells, and water electrolysis. In particular, metal–air batteries require multiple catalysts for the ORR and OER. Thus, bifunctional catalysts are required to improve efficiency and simplify catalytic systems. Hence, we developed defect- and oxygen-rich nanocarbons as bifunctional catalysts through a one-pot formation by applying plasma discharge in mixed solvents of benzene with crown ether. Raman and X-ray photoelectron spectroscopy results confirmed that oxygen was embedded and functionalized into the carbon matrix and abundant defects were formed, which highly affected the catalytic activity of the ORR and OER. The obtained CNP-CEs revealed a tuned electron transfer trend to a rapid four-electron pathway (n = 3.5) for the ORR, as well as a decreased onset potential and Tafel slope for the OER. Consequently, CNP-CE-50 exhibited an improved bifunctional catalytic characteristic with the narrowest potential gap between the ORR and OER. We believe that our findings suggest new models for carbon-based bifunctional catalysts and provide a prospective approach for a synthetic procedure of carbon nanomaterials.

1. Introduction

To overcome global warming, new technologies are required for renewable and environment-friendly energy systems. Recently, studies on energy storage and conversion devices, including fuel cells, secondary batteries, metal–air batteries, and water electrolysis have been attempted and increased progressively.[1–5] To improve the efficiency of the aforementioned devices, appropriate catalysts are required for applications. In addition, several devices require multiple catalysts for different reactions between the cathode and anode. Thus, simultaneously useable bifunctional catalysts could improve the performance and economic efficiency of cathode and anode reactions.

Metal–air batteries are driven by continuous reactions between the cathode and anode. To enhance their performance, catalysts are required for the oxygen reduction reaction (ORR) and oxygen evolution reaction (OER) at the cathode and anode, respectively. Nanostructured Pt and RuO_2 or IrO_2 are considered the best catalysts for the ORR and OER, respectively.[6–8] However, limited resources and their high cost can diminish their performance merits. In addition, the agglomeration, sintering, and decomposition of catalysts occur during long-term operation. Thus, to resolve these drawbacks, heteroatom-doped carbon-based materials are considered effective metal-free catalysts.[9,10] Doping has been attempted using nitrogen, boron, phosphorus, sulfur, oxygen, and fluorine to improve catalytic activity.[11–15] Heteroatom-doped carbon reduces oxygen molecules through the following mechanism. Owing to a difference in electronegativity and the atomic radius, the charge neutrality is broken, and neighboring sites enter the charge-delocalized state with defects, which can be active sites.[11,16,17]

In the case of oxygen as a dopant, its high electronegativity, compared with that of carbon, could reveal a behavior similar to that of other dopants. Moreover, oxygen-containing functional groups with abundant defects can efficiently adsorb oxygen molecules and oxygenated intermediates, which would facilitate the ORR and OER.[18,19] Various approaches have been employed to introduce oxygen-containing functional groups into the carbon matrix.[14,18,20,21] Among these approaches, the oxygen plasma treatment is the most used. Due to oxygen plasma, the oxygen contents are effectively doped or functionalized, which increases catalytic activity.[14,18] Although this is an effective route to enhancing catalytic activity, multiple steps (carbon material synthesis and plasma modification) are required in a vacuum environment. *Via* another route, chemical synthesis is also applied using oxygen-containing organic

---

[a] *Department of Materials Chemistry, Shinshu University, 4-17-1, Wakasato, Nagano, 3808553, Japan*

[b] *Advanced Manufacturing Process R&D Group, Ulsan Regional Division, Korea Institute of Industrial Technology (KITECH), 55, Jongga-ro, Jung-gu, Ulsan, 44313, Korea. E-mail: dwkim@kitech.re.kr*

† Electronic supplementary information (ESI) available. See DOI: **https://doi.org/10.1039/d3ra05164a**

molecules. However, this alternative route requires template materials and oxidation steps with a long processing time.[21]

Hence, we employed a prospective synthesis method, named the solution plasma process (SPP), for oxygen-embedded and -functionalized nanocarbon materials. Solution plasma is a type of nonequilibrium and cold plasma in the liquid phase. During discharge, highly active species and energetic electrons promote rapid reaction kinetics.[22–25] SPP has been employed to synthesize nanocarbon, metal oxide, and nanocomposites.[26–28] Here, SPP was applied in an 18-crown-6 ether-added benzene precursor to embed and functionalize oxygen into the inside and edge of the carbon structure with abundant defects. The products were synthesized through the dissociation and recombination of benzene and 18-crown-6 ether. The obtained catalysts exhibited improved catalytic activity in the ORR and OER. The effect of introduced oxygen and defect sites on the bifunctional catalytic activity and their role was investigated. Thus, this report provides a route to the rational design of bifunctional catalysts using oxygen functional groups in the carbon matrix.

2. Experimental

2.1 Material synthesis

Defect and oxygen-rich nanocarbon was synthesized by SPP in mixed oxygen-containing organic solvents. Benzene (C_6H_6, Kanto Chemical) and dicyclohexano-18-crown-6 ether ($C_{20}H_{36}O_6$, crown ether (CE), Tokyo Chemical Industry) were used as carbon and oxygen sources, respectively. To control the oxygen content with defects, various CE concentrations (10, 20, and 50 mM) were added to the benzene solvents. The obtained particles were denoted CNP-CE-10, CNP-CE20, and CNP-CE50, respectively. Pure carbon, CNP, was compared as a reference.

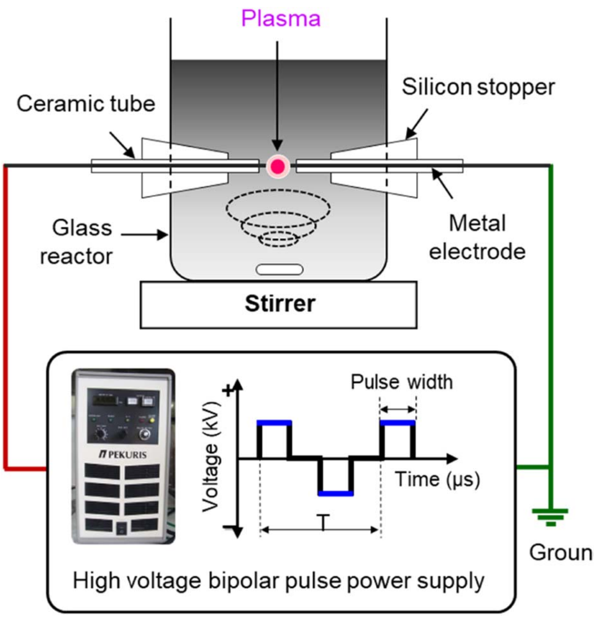

Fig. 1 Schematic illustration of the solution plasma process setup.

To generate solution plasma, a pair of tungsten rods (outer diameter (o.d.), 1 mm) were used as the electrodes, and a voltage of 1.2 kV was applied using a bipolar pulsed power generator (MPP04, Kurita) for 10 min. The pulse width and frequency were fixed to 0.8 μs and 25 kHz, respectively. The schematic experimental setup is shown in Fig. 1. After plasma discharge, the obtained suspension was filtrated and dried in a vacuum oven at 80 °C for 24 h.

2.2 Characterization

The structural properties were analyzed by X-ray diffraction (XRD; ULTIMA 4, Rigaku) with Cu Kα ($\lambda = 1.5418$ Å) and Raman spectroscopy (NEXSA, Thermo Scientific) with 532 nm laser power. To investigate the morphologies of the obtained materials, field-emission scanning electron microscopy (FE-SEM; SU8020, Hitachi) and transmission electron microscopy (TEM; JEL-2100F, JEOL) were performed. The specific surface area and pore structure were observed by nitrogen adsorption/desorption isotherms (3-Flex, Micromeritics) using the Brunauer–Emmett–Teller (BET) and Barrett–Joyner–Halenda (BJH) methods. X-ray photoelectron spectroscopy (XPS; NEXSA, Thermo Scientific, monochromatic Al Kα) was conducted to examine the surface chemical compositions and chemical bonding. The electrical resistivity was conducted by four-point probe method (CMT-SR1000N, AIT).

2.3 Electrochemical measurements

Electrochemical measurements were conducted using a multi-potentiostat (ZIVE MP2A, WonATech) with a three-electrode system. Pt wire, Ag/AgCl, and glassy carbon were used as the counter, reference, and working electrodes, respectively. To prepare the working electrode, 20 μL of catalyst ink was drop-cast onto the glassy carbon. Typically, the catalyst (5 mg) was dispersed in ethanol (0.5 mL), and a Nafion ionomer (50 μL, 5 wt%, Sigma Aldrich) was added. The mixture was sonicated for 30 min to obtain homogeneous ink. To examine the ORR and OER activity, cyclic voltammetry (CV) and linear sweep voltammetry (LSV) were performed. The CV curves were obtained within a range of −1.0 to 0.3 V (V *vs.* Ag/AgCl) at a scan rate of 20 mV s^{-1} in N_2- and O_2-saturated 0.1 M KOH. LSV measurements were conducted for the ORR and OER using a rotating disk electrode (RDE) at the scan rate of 10 mV s^{-1} with a rotation speed of 2000 rpm in the ranges of −1.0 to 0.2 V and 0.2–1.0 V (V *vs.* Ag/AgCl), respectively.

3. Results and discussion

3.1 Synthetic mechanism

We previously reported that the formation of nanocarbon particles was achieved *via* the dissociation and reconstruction reaction in aromatic hydrocarbon solvents. Owing to plasma discharge, energetic electrons and reactive species decompose solvents, and generated radicals, such as C_2 and CH, reconstruct with the surrounding intermediates.[25,29] To introduce oxygen and create defects, CE was used as an oxygen precursor with a defect promoter. The CE was decomposed and generated

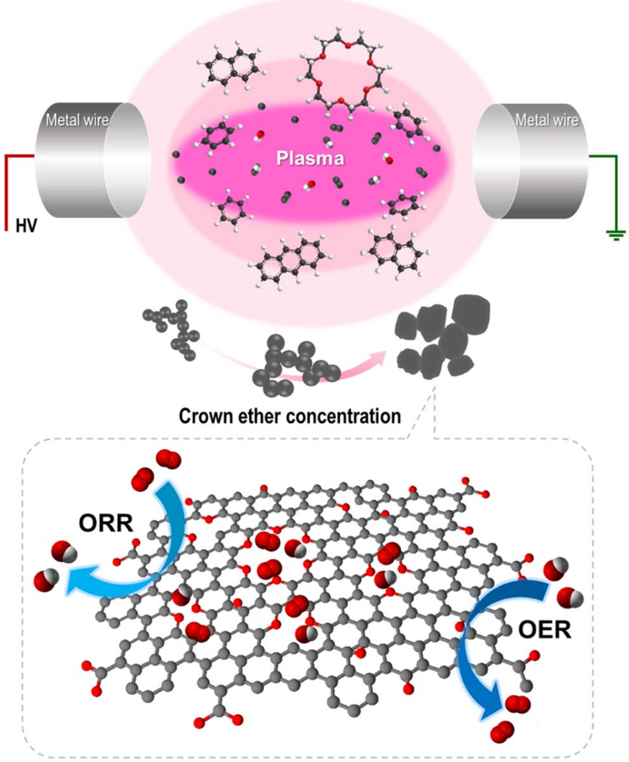

Fig. 2 Proposed synthetic mechanism of Defect and oxygen-rich nanocarbon.

radicals, including O, C_2, H, and CH, in the plasma core region. Simultaneously, the oxygen-containing intermediates derived from CE decomposition incorporated into carbon matrix and functionalized on the edge of carbon. Furthermore, it did not completely decompose, thereby generating partially decomposed and only C–H-activated cationized CE because of the low energy at the plasma/liquid interface. The activated CE was also reconstructed with small polycyclic aromatic hydrocarbon and incorporated into carbon matrix. Thus, the oxygen was embedded and functionalized with numerous defects within the carbon matrix. The proposed synthetic mechanism is shown in Fig. 2. To clarify this hypothesis, the chemical bonding structure and structural deformation were investigated.

3.2 Characterization

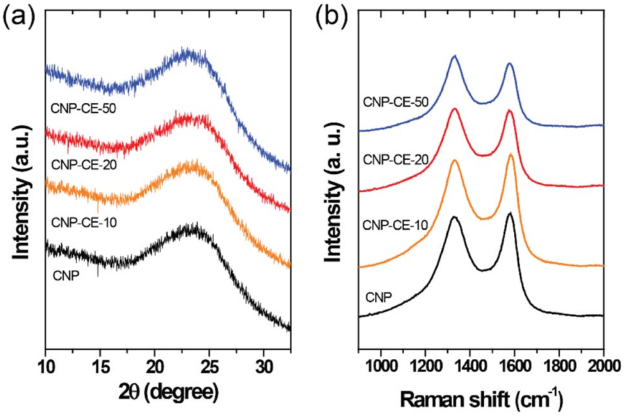

Fig. 3 (a) XRD patterns and (b) Raman spectra of CNP and CNP-CEs.

The structural characteristics were investigated by XRD and Raman measurements. The XRD patterns of the CNP and CNP-CEs are shown in Fig. 3a. The graphitic carbon (002) diffraction was mainly focused to confirm the degree of graphitization. With an increase in CE concentration, the (002) diffraction peak slightly broadened, whereas the peak position of the (002) diffraction slightly shifted toward a lower 2θ angle. The expansion of the interplanar spacing (d_{002}) might have originated from the oxygen with defects incorporated into the carbon lattice. The increased CE further induced deformation in the carbon structure. Fig. 3b shows the Raman spectra of the CNP and CNP-CEs as a function of the CE concentration. As expected, CNP exhibited the lowest I_D/I_G value among all the prepared particles. Due to the addition of CE, the I_D/I_G value gradually increased with an increase in CE. CNP-CE-50 exhibited the highest I_D/I_G value, which significantly increased compared with that of CNP. The D peak corresponded to a distortion of the graphitic lattice;[30] therefore, a high I_D/I_G value implied more defects within the carbon matrix. In addition, the average defect distance (L_D) and defect density (n_D) were calculated using the following equation.[31,32]

$$L_D{}^2\ (\mathrm{nm}^2) = 1.8 \times 10^{-9} \lambda_L{}^4\ (I_D/I_G)^{-1}$$

$$n_D\ (\mathrm{cm}^{-2}) = \frac{1.8 \times 10^{22}}{\lambda_L{}^4}\left(\frac{I_D}{I_G}\right)$$

where λ_L is the excitation laser wavelength of the Raman laser source. These equations were valid for point defects rather than edge defects. The calculated L_D and n_D with the I_D/I_G values are summarized in Table 1. Due to an increase in the CE concentration, the L_D and n_D decreased and increased, respectively, suggesting the formation of more defects within the carbon matrix. The obtained results were consistent with the XRD results, confirming that the oxygen atoms were successfully embedded and functionalized into the carbon matrix and led to the formation of abundant defects. The embedment of hetero atoms and numerous defect sites could affect electronic structure of CNP. To clarify these effects, the electrical resistivity was examined. As reference, CNP exhibited 84 Ω cm. Owing to introduce CE, the resistivity was slightly decreased to 70 Ω cm at CNP-CE-50. The resistivity values of CNP-CE-10 and -20 were 79

Table 1 Deformation parameters calculated from Raman spectra

Samples	I_D/I_G	L_D (nm)	n_D (cm^{-2})
CNP	0.88	12.80	1.97×10^{11}
CNP-CE-10	0.94	12.38	2.11×10^{11}
CNP-CE-20	1.01	11.94	2.26×10^{11}
CNP-CE-50	1.04	11.77	2.34×10^{11}

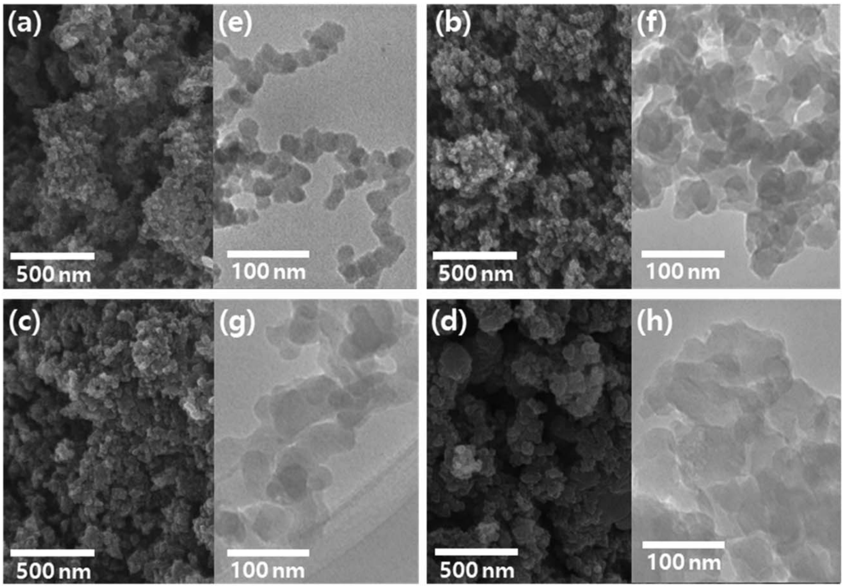

Fig. 4 FE-SEM and TEM images of CNP (a, e), CNP-CE-10 (b, f), CNP-CE-20 (c, g), and CNP-CE-50 (d, h).

and 76 Ω cm, respectively. The improved conductivity could contribute to catalytic activity.

The morphology of the CNP and CNP-CEs was investigated by electron microscopy. FE-SEM images (Fig. 4a–d) revealed that the CNP and CNP-CEs exhibited homogeneous shape and size distribution. TEM images (Fig. 4e–h) showed that the particle size gradually increased with an increase in the CE concentration from *ca.* 20 nm to *ca.* 60 nm. In addition, their spherical-like shape began to slowly transform into a sheet-like shape with the addition of CE. These morphological changes might be originated from the generated O radicals and cationized CE during plasma discharge. During reconstruction, partially decomposed and C–H-activated CE was polymerized with polycyclic aromatic hydrocarbon intermediates, and O radicals induced more hexagon ring structures, resulting in gradual growth into a sheet-like structure.[25,33]

The effect of the morphological features on the specific surface area (SSA) with the pore structure was investigated using the BET method (Fig. S1†). The measured SSA values are summarized in Table S1.† The SSA and pore volume of CNP were 149 m^2 g^{-1} and 1.57 cm^3 g^{-1}, respectively. The addition of CE slightly increased the SSA and pore volume to 169–173 m^2 g^{-1} and 1.77–1.83 cm^3 g^{-1}, respectively, which might be attributed to the creation of several defects in the matrix.

XPS analysis was performed to investigate the chemical bonding and the effect on active sites (Fig. 5). In the survey spectra, carbon and oxygen peaks were detected without any element, and the chemical composition changed with the CE concentration (Fig. 5a). In the C 1s core-level spectra (Fig. 5b), the spectra were deconvoluted into five peaks, which were assigned to C═C (284.4 ± 0.2 eV), C–C/C–H (285.3 ± 0.2 eV), C–O (286.4 ± 0.2 eV), C═O (287.4 ± 0.2 eV), and O–C═O (288.8 ± 0.2 eV).[34] Due to the addition of CE, the sp^3 carbon bond relatively increased compared with that of CNP. The ratio of sp^3 carbon increased with an increase in CE. An association between decomposed C_2 radicals and CE intermediates during the discharge might have caused an increase in sp^3 hybridization. Fig. 5c shows the O 1s core-level spectra. The three

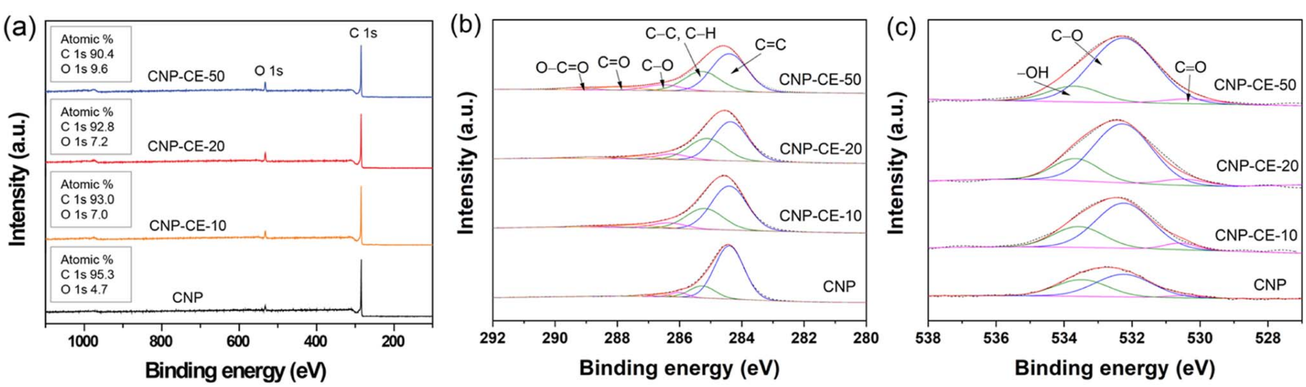

Fig. 5 XPS spectra of CNP and CNP-CEs (a) survey, (b) C 1s, and (c) O 1s.

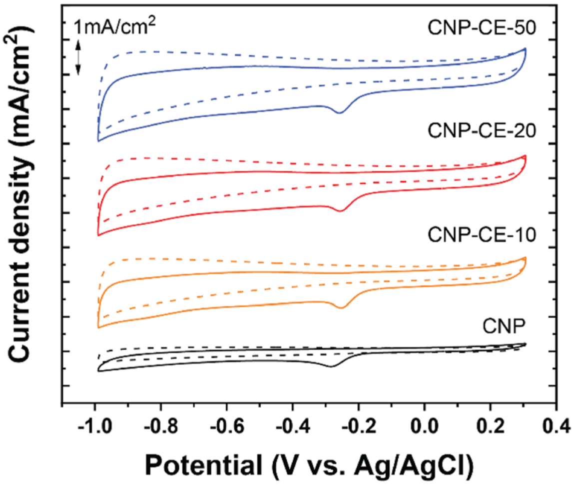

Fig. 6 Cycle voltammetry curves of CNP and CNP-CEs at a scan rate of 20 mV in the N_2 and O_2 saturated 0.1 M KOH.

deconvoluted peaks were assigned to –OH (533.7 ± 0.3 eV), C–O (532.2 ± 0.3 eV), and C=O (530.3 ± 0.3 eV).[35] With an increase in the CE concentration, the bonding ratio changed, which tended to increase the C–O bonding from 57 to 78%. The –OH species decreased from 39 to 19%. The increase in C–O bonding might arise from the embedded and functionalized ether groups derived from the CE molecules. The XPS core-level results revealed good agreement between the C 1s and O 1s spectra. The increased embedded and functionalized oxygen could be an active site for the ORR, which might facilitate electrocatalytic reactions.[36,37]

3.3 Electrochemical characteristics

To investigate catalytic activity toward the ORR, CV was conducted in an N_2- and O_2-saturated 0.1 M KOH electrolyte at a scan rate of 20 mV s^{-1} (Fig. 6). A cathodic peak and onset potential corresponding to the ORR were detected at −0.285 and −0.193 V, respectively, for CNP (Fig. 6). Due to the addition of CE, oxygen-embedded and -functionalized sites with abundant defects were formed within the carbon matrices, which highly affected the ORR activity. Compared with CNP, the CNP-CEs exhibited significantly enhanced ORR catalytic activity. The cathodic peak and onset potential were shifted to higher potentials of −0.254 and −0.154 V, respectively. Furthermore, the current density of the ORR for CNP-CE-50 was more than two times higher than that of CNP. Among the CNP-CEs, the ORR potential had similar values, whereas the current density gradually increased with an increase in CE. The results suggested that increasing the CE led to increased active sites for the ORR, which promoted higher current density. In addition, numerous defects formation could affect to enhance

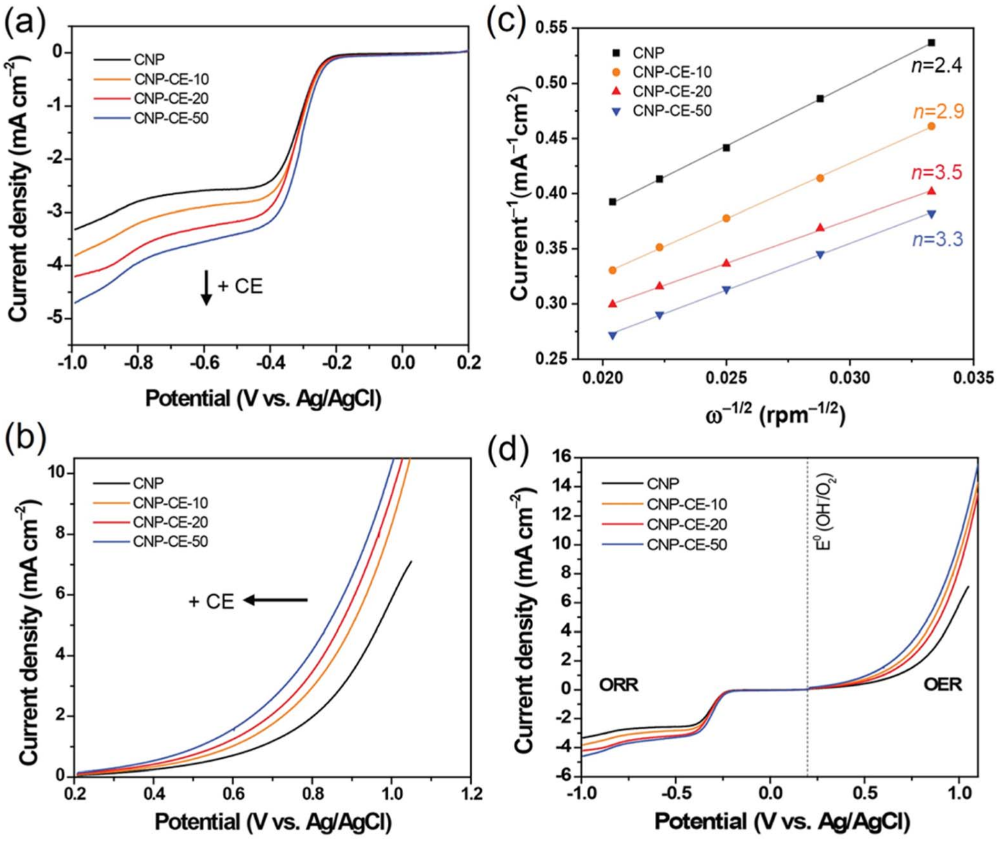

Fig. 7 Linear sweep voltammograms of CNP and CNP-CEs for (a) ORR and (b) OER, (c) Koutecky–Levich (K–L) plots, and (d) overall catalytic activity at a scan rate of 10 mV in the O_2 saturated 0.1 M KOH.

electrochemical active surface area (ECSA), which contribute to higher ORR current density (Fig. S2†). Note that the pure CE was did not show any peaks related ORR due to lack of ECSA (Fig. S3†).

To elucidate the electron transfer kinetics during the ORR, LSV was conducted in the O_2-saturated 0.1 M KOH solution at a scan rate of 10 mV and different rotation speeds using an RDE. The measured all of LSV results are shown in Fig. S4.† As shown in Fig. 7a, the limiting current density of the CNP-CEs increased with an increase in CE from 10 to 50 mM, which was consistent with the CV results. During the ORR process, the electron transfer number (n) was determined using the Koutecký–Levich (K–L) equation.[38]

$$\frac{1}{j} = \frac{1}{j_{\mathrm{L}}} + \frac{1}{j_{\mathrm{k}}}$$

$$\frac{1}{j} = \frac{1}{B\omega^{1/2}} + \frac{1}{j_{\mathrm{k}}}$$

$$B = 0.2nFC_0^* D_0^{2/3} \nu^{-1/6}$$

where j is the measured current density; j_{k} and j_{L} are the kinetic and diffusion-limiting current densities, respectively; ω is the disk rotation rate; n is the number of electrons transferred per oxygen molecule; F is Faraday's constant ($F = 96\,485$ C); n is the number of electrons transferred per oxygen molecule; C_0^* and D_0 are the oxygen bulk concentration (1.2×10^{-6} mol cm^{-3}) and diffusion coefficient of oxygen (1.9×10^{-5} cm^2 s^{-1}), respectively; and ν is the kinetic viscosity of the electrolyte (1.1×10^{-2} cm^2 s^{-1}).[39,40] The K–L plots revealed good linearity for all the samples, and n was calculated from the slope of the K–L plots (Fig. 7c). The calculated n of CNP was 2.4 at −0.5 V, which was close to the two-electron transfer process. Contrarily, the CNP-CEs exhibited an ORR process close to the four-electron transfer. This verified that the presence of oxygen-embedded and -functionalized sites and defects within the carbon matrices significantly improved the reaction kinetics and activity for ORR.

Interestingly, the highest n of 3.5 was observed for CNP-CE-20. This unexpected result might be originated from the oxygen content of the carbon matrices. According to previous studies, oxygen-containing functional groups frequently induce to produce hydrogen peroxide, which led to a two-electron transfer process as a dominant pathway.[40,41] The XPS results indicated significant increasing oxygen contents when CE was increased from 20 to 50 mM. Thus, CNP-CE-50 involved more two-electron reactions than CNP-CE-20, resulting in a reduced n value. Although the n value was reduced, CNP-CE-50 exhibited mainly four-electron transfer processes and the highest limiting current density. An increase in CE induced the formation of more defects, which allowed more adsorption for the oxygen molecules.[42–44] Consequently, high oxygen accessibility with abundant defect sites led to the utilization of more active sites and increased the reaction capacity for the ORR, which would cause a progressive increasing of the current density for CNP-CE-50.

The OER activity was examined to investigate bifunctional catalytic activity (Fig. 7b). As shown in Fig. 7b, the CNP-CEs revealed smaller onset potentials and faster elevating current densities for the OER than that of CNP. The onset potential gradually decreased with an increase in CE. Moreover, Tafel slope of CNP-CE-50 exhibited the lowest value in the prepared catalysts, indicating low overpotential, and it tends to same tendency with onset potential (Fig. S5†). This trend for the OER activity of CNP-CEs might be originated from the concentration of oxygen atoms and defects in the carbon matrix. Owing to the embedded and functionalized oxygen atoms, the surrounding site became an uneven electric charge state.[14,39] Thus, the neighboring carbon atoms were positively charged by the charge redistribution.[17,39] The conjugated oxygen atoms led to a positive charge, thus the neighboring carbon can be an active site for OER. The positively charged carbon facilitated the adsorption of the surrounding OH− by electrostatic forces, which efficiently evolved oxygen molecules during the OER.[45] To determine the bifunctional catalytic characteristic, the potential gap (ΔE) between the ORR (at −3 mA cm^{-2}) and OER (at 10 mA cm^{-2}) potentials was investigated (Fig. 7d). The ΔE can be explained by the sum of overpotentials for the ORR and OER. A narrow ΔE is a criterion for determining the bifunctional catalytic characteristic. As explained, the CNP-CEs exhibited improved catalytic activity in the ORR and OER. Thus, CNP-CE-50 revealed the narrowest ΔE in the prepared all the catalyst.

Based on the aforementioned results, the addition of CE during discharge facilitated the embedment and functionalization of oxygen within the carbon matrices, which could be effective active sites for the ORR and OER. In addition, an appropriate concentration of oxygen is a critical factor for the ORR. Moreover, the formation of abundant defects facilitated the adsorption of oxygen molecules and hydroxide species, which affected to enhance bifunctional catalytic activity.

4. Conclusions

Defect and oxygen-rich nanocarbon was successfully synthesized *via* plasma discharge in benzene with CE. Due to the dissociation and recombination of benzene and CE, the oxygen-containing species were embedded and functionalized into the carbon matrix. Raman spectroscopy results demonstrated that the added CE effectively created defect sites. The synergetic effect between the embedded and functionalized oxygen with defects ensured sufficient catalytic activity for the ORR and OER. Moreover, the CNP-CEs presented mainly a four-electron transfer process for the ORR, and CNP-CE-20 revealed the highest n of 3.5. Besides, an added CE led to a low overpotential with a high current density for the OER. We expect that defect and oxygen-rich nanocarbon will be a new route for synthesizing bifunctional catalysts and carbon-based functional materials.

Conflicts of interest

There are no conflicts to declare.

Acknowledgements

This research was supported by Korea Research Fellowship program funded by the Ministry of Science and ICT through the National Research Foundation of Korea (2019H1D3A1A01071089). This study has been conducted with the support of the Korea Institute of Industrial Technology as "Support Business of Customized Production Technology for Small and Medium Enterprises (KITECH UR-23-0049)".

References

1 M. K. Singla, P. Nijhawan and A. S. Oberoi, *Environ. Sci. Pollut. Res. Int.*, 2021, **28**, 15607–15626.

2 N. Zhang, T. Deng, S. Zhang, C. Wang, L. Chen, C. Wang and X. Fan, *Adv. Mater.*, 2022, **34**, e2107899.

3 N. Sharmili, R. Nagi and P. F. Wang, *J. Energy Storage*, 2023, **68**, 107622.

4 S. S. Kumar and H. Lim, *Sustainable Energy Fuels*, 2023, **7**, 3560–3583.

5 R. Bianqing, J. Cao, H. Zhang, C. Han and W. Xu, *Mater. Chem. Front.*, 2023, **7**, 3209–3231.

6 M. Liu, Z. Zhao, X. Duan and Y. Huang, *Adv. Mater.*, 2019, **31**, 1802234.

7 Z. Ma, Y. Zhang, S. Liu, W. Xu, L. Wu, Y.-C. Hsieh, P. Liu, Y. Zhu, K. Sasaki and J. N. Renner, *J. Electroanal. Chem.*, 2018, **819**, 296–305.

8 H. Over, *ACS Catal.*, 2021, **11**, 8848–8871.

9 J. Quílez-Bermejo, E. Morallón and D. Cazorla-Amorós, *Carbon*, 2020, **165**, 434–454.

10 H. Shi, Y. Shen, F. He, Y. Li, A. Liu, S. Liu and Y. Zhang, *J. Mater. Chem. A*, 2014, **2**, 15704–15716.

11 D. Guo, R. Shibuya, C. Akiba, S. Saji, T. Kondo and J. Nakamura, *Science*, 2016, **351**, 361–365.

12 M. Del Cueto, P. Ocón and J. Poyato, *J. Phys. Chem. C*, 2015, **119**, 2004–2009.

13 Y. Sun, J. Wu, J. Tian, C. Jin and R. Yang, *Electrochim. Acta*, 2015, **178**, 806–812.

14 R. Mohan, A. Modak and A. Schechter, *ACS Sustain. Chem. Eng.*, 2019, **7**, 11396–11406.

15 Y. Chang, J. Chen, J. Jia, X. Hu, H. Yang, M. Jia and Z. Wen, *Appl. Catal., B*, 2021, **284**, 119721.

16 S. K. Singh, K. Takeyasu and J. Nakamura, *Adv. Mater.*, 2019, **31**, 1804297.

17 J. Quílez-Bermejo, E. Morallón and D. Cazorla-Amorós, *Carbon*, 2020, **165**, 434–454.

18 L. Q. Li, H. B. Yang, J. W. Miao, L. P. Zhang, H. Y. Wang, Z. P. Zeng, W. Huang, X. C. Dong and B. Liu, *Appl. Catal., B*, 2017, **2**, 294–300.

19 S. W. Ham, H. P. Hong, J. H. Kim, S. J. Min and N. K. Min, *J. Nanosci. Nanotechnol.*, 2014, **14**, 8476–8481.

20 S. Ghosh, S. Barg, S. M. Jeong and K. Ostrikov, *Adv. Energy Mater.*, 2020, **10**, 20011239.

21 Z. X. Chen, Y. Z. Li, M. Wu and Y. L. Cao, *Energy Fuel*, 2021, **35**, 2665–2673.

22 O. Takai, *Pure Appl. Chem.*, 2008, **80**, 2003–2011.

23 M. A. Bratescu, S.-P. Cho, O. Takai and N. Saito, *J. Phys. Chem. C*, 2011, **115**, 24569–24576.

24 C. Chokradjaroen, X. Wang, J. Niu, T. Fan and N. Saito, *Mater. Today Adv.*, 2022, **14**, 100244.

25 T. Morishita, T. Ueno, G. Panomsuwan, J. Hieda, A. Yoshida, M. A. Bratescu and N. Saito, *Sci. Rep.*, 2016, **6**, 36880.

26 D. W. Kim, O. L. Li and N. Saito, *Phys. Chem. Chem. Phys.*, 2015, **17**, 407–413.

27 H. Kim, A. Watthanaphanit and N. Saito, *ACS Sustain. Chem. Eng.*, 2017, **5**, 5842–5851.

28 H. M. Kim, N. Saito and D. W. Kim, *Chemistryselect*, 2018, **3**, 6302–6308.

29 N. Saito, M. A. Bratescu and K. Hashimi, *Jpn. J. Appl. Phys.*, 2018, **57**, 0102A4.

30 K. Ghosh, M. Kumar, T. Maruyama and Y. Ando, *Carbon*, 2009, **47**, 1565–1575.

31 L. G. Cançado, A. Jorio, E. M. Ferreira, F. Stavale, C. A. Achete, R. B. Capaz, M. V. d. O. Moutinho, A. Lombardo, T. Kulmala and A. C. Ferrari, *Nano Lett.*, 2011, **11**, 3190–3196.

32 M. M. Lucchese, F. Stavale, E. M. Ferreira, C. Vilani, M. V. d. O. Moutinho, R. B. Capaz, C. A. Achete and A. Jorio, *Carbon*, 2010, **48**, 1592–1597.

33 R. Singh and M. Frenklach, *Carbon*, 2016, **101**, 203–212.

34 Y. Yamada, K. Murota, R. Fujita, J. Kim, A. Watanabe, M. Nakamura, S. Sato, K. Hata, P. Ercius and J. Ciston, *J. Am. Chem. Soc.*, 2014, **136**, 2232–2235.

35 J. Masa, C. Batchelor-McAuley, W. Schuhmann and R. G. Compton, *Nano Res.*, 2014, **7**, 71–78.

36 B. Narayanamoorthy, K. Datta and S. Balaji, *J. Colloid Interface Sci.*, 2012, **387**, 213–220.

37 S. Brocato, A. Serov and P. Atanassov, *Electrochim. Acta*, 2013, **87**, 361–365.

38 L. Xie, W. Zhou, Z. Qu, Y. Ding, J. Gao, F. Sun and Y. Qin, *J. Colloid Interface Sci.*, 2022, **610**, 934–943.

39 J. Gu, J. Xie, S. Li, G. Song and M. Zhou, *Chem. Eng. J.*, 2023, **452**, 139597.

40 X. Xie, L. Du, L. Yan, S. Park, Y. Qiu, J. Sokolowski, W. Wang and Y. Shao, *Adv. Funct. Mater.*, 2022, **32**, 2110036.

41 Y. Jia, L. Zhang, A. Du, G. Gao, J. Chen, X. Yan, C. L. Brown and X. Yao, *Adv. Mater.*, 2016, **28**, 9532–9538.

42 D. Guo, R. Shibuya, C. Akiba, S. Saji, T. Kondo and J. Nakamura, *Science*, 2016, **351**, 361–365.

43 Y. Jiao, Y. Zheng, K. Davey and S.-Z. Qiao, *Nat. Energy*, 2016, **1**, 1–9.

44 X. Lu, W.-L. Yim, B. H. Suryanto and C. Zhao, *J. Am. Chem. Soc.*, 2015, **137**, 2901–2907.

45 H. B. Yang, J. Miao, S.-F. Hung, J. Chen, H. B. Tao, X. Wang, L. Zhang, R. Chen, J. Gao and H. M. Chen, *Sci. Adv.*, 2016, **2**, e1501122.